Divergence and curl of the inertial particle velocity in a four-way coupled turbulent channel flow

By J. R. West, T. Oujia‡, K. Matsuda¶, K. Schneider‡, S. S. Jain AND K. Maeda

Inertial particle data from three-dimensional direct numerical simulations of dilute, four-way coupled particle-laden turbulent channel flow at $Re_\tau \approx 230$ are analyzed. Delaunay tessellation is applied to the particle positions considering a range of mass loading $(10-100\%)$. Using finite-time measures, we then quantify the divergence and rotation of the particle velocity using the methods in Oujia *et al.* (2020, 2022a). Statistical analyses of divergence and curl are performed, along with their dependence on the wall distance, to assess the influence of the flow anisotropy. Divergence and curl fluctuations are most intense in the buffer layer due to the stronger fluctuations of fluid velocity there. The probability density functions (PDFs) of the divergence and curl show that the particle inertia gives heavier tails to the PDFs, implying extreme events. The greatest effect of mass loading is observed in the viscous sublayer, where substantial damping in divergence and curl fluctuations is observed as mass loading is increased.

1. Introduction

Particle-laden turbulent flows over walls occur in many natural and engineered systems. Examples include sediment transport in rivers, dust storms in the atmospheric boundary layer (Hutter 2005), and chemical processes in industrial riser reactors (Basu 2006). In all of these examples, particles are transported by the flow and exert drag forces back on the flow. Experiments by Kulick *et al.* (1994) showed that that at sufficient mass loading, the particle phase can significantly attenuate the fluid turbulence in channel flow. Because of their finite inertia, particles preferentially concentrate in regions of low vorticity and high strain, leading to complex dynamics of clusters (Squires & Eaton 1991). Sweeps and ejections in wall turbulence play an important role in cluster dynamics and near-wall accumulation in particle-laden channel flow (Marchioli & Soldati 2002). Clustering also affects the optical depth in gas flows laden with heavy particles, which is important in the design of particle-based solar receivers (Pouransari & Mani 2016) and in radiation absorption in clouds (Matsuda *et al.* 2012). The complex physics of particle collisions, combined with the strong flow modifications that occur at large mass loading, makes these flows difficult to predict. In addition, the optical depth makes them difficult to study experimentally, making simulations an attractive way to improve our understanding.

An essential tool for analyzing particle-clustering statistics is tessellation. Monchaux *et al.* (2010) used Voronoi tessellation to characterize the dependence of clustering on Stokes number. This technique has been largely applied in homogeneous isotropic turbulence,

‡ Institut de Mathématiques de Marseille, Aix-Marseille Universit, CNRS, France
¶ Japan Agency for Marine-Earth Science and Technology (JAMSTEC), Japan

but a few studies have applied it to wall-bounded flows. For example, Nilsen *et al.* (2013) confirmed the nonmonotonic behavior of clustering with respect to Stokes number in channel flow using Voronoi tessellation in wall-parallel slices of the domain. To gain further insight into the dynamics of particle clouds, gradient information of the particle velocity could be used. For instance, the divergence of the particle velocity quantifies structure formation in particle clouds, i.e., voids and clusters. However, because particle velocities are only defined at particle positions, there is an inherent difficulty in using standard spatial differential operators to compute the gradient information. Oujia *et al.* (2020) proposed a method for quantifying the divergence using tessellation of particle positions. The time change of the tessellation cell volume was shown to yield a measure of the divergence of the particle velocity. A method for computing the curl of the particle velocity was then introduced in Oujia *et al.* (2022a) in order to quantify rotation of particle clouds.

The goal of the current work is twofold. First, we present the Direct Numerical Simulation (DNS) data of a four-way coupled channel flow for different mass loading, and briefly characterize the effect of mass loading on the mean flow and turbulent fluctuations, in comparison with the channel flow data without particles. Second, we apply the tessellation-based method to determine the divergence and curl of the inertial particle velocity. With that, we investigate the void/cluster formation and the rotation/swirling motion of particles in different flow regions: the viscous sublayer, the buffer layer, and the logarithmic region.

2. Governing equations and the four-way coupled channel flow data

The channel flow data analyzed in this work was obtained using the Soleil-MPI code, which is briefly described here; more details on this code can be found in Esmaily *et al.* (2020). The Navier-Stokes equations for incompressible flow with particle two-way coupling terms are solved as

$$\frac{\partial\left(\rho \boldsymbol{u}\right)}{\partial t}+\nabla\cdot\left(\rho \boldsymbol{u}\otimes \boldsymbol{u}\right)=-\nabla p+\mu\nabla^2\boldsymbol{u}+\sum_{m=1}^{N_p}\boldsymbol{f}^{(m)}\delta(\boldsymbol{x}-\boldsymbol{x}^{(m)}), \tag{2.1}$$

where $\boldsymbol{u}$ is the fluid velocity, ρ is the (constant) fluid density, p is the hydrodynamic pressure, and μ is the dynamic viscosity. The last term is the summation of the two-way coupling force contribution from each particle $\boldsymbol{f}^{(m)}$, over all particles N_p, based on the Dirac-delta function $\delta(\cdot)$, which has units of inverse volume and whose argument is the distance between a position in the fluid $\boldsymbol{x}$ and a given particle $\boldsymbol{x}^{(m)}$. Because the focus in this work is on flows with a small total volume fraction (all below 1.5×10^{-4}), the volume displacement effect has been ignored. The particle drag force is the drag correlation for finite Reynolds numbers from Schiller & Naumann (1935)

$$\boldsymbol{f}^{(m)}=3\pi\mu D_p\left(1+0.15Re_p^{0.687}\right)\left(\boldsymbol{v}_p^{(m)}-\widetilde{\boldsymbol{u}}^{(m)}\right), \tag{2.2}$$

where D_p is the particle diameter, $\boldsymbol{v}_p^{(m)}$ is the velocity of particle m, $\widetilde{\boldsymbol{u}}^{(m)}$ is the undisturbed fluid velocity at the particle location, and Re_p is the particle Reynolds number.

Soleil-MPI solves the above equations using a finite-volume method with second-order explicit spatial derivatives. At each time step, a pressure Poisson equation is solved numerically using a geometric multigrid method to guarantee mass conservation. The two-way-coupling terms in the momentum equations are obtained by distributing the

	Re_τ	N_p	ϕ_0	St^+
Flow 0	229	0	0	N/A
Flow 1	225	1.43×10^7	0.1	6.90
Flow 2	227	5.70×10^7	0.4	7.01
Flow 3	234	1.43×10^8	1.0	7.45

TABLE 1. Parameters of the channel flow data: the friction Reynolds number Re_τ, the number of particles N_p, the overall mass loading ϕ_0, and the friction Stokes number St^+. The density ratio between particle and fluid is $8900/1.2 \approx 7417$.

force associated with each particle among the surrounding grid points using trilinear interpolation, using the correction scheme proposed by Esmaily & Horwitz (2018) to account for particle disturbances on the fluid velocity.

Each particle trajectory is computed according to the equations of motion for a single particle of mass m_p, neglecting gravity

$$\dot{\boldsymbol{x}}_p{}^{(m)} = \boldsymbol{v}_p^{(m)}, \tag{2.3}$$

$$m_p \dot{\boldsymbol{v}}_p{}^{(m)} = -\boldsymbol{f}^{(m)}. \tag{2.4}$$

Time advancement for both the Eulerian fluid variables and the Lagrangian point particles is done with a second-order Runge-Kutta method. Collisions with walls and other particles are accounted for assuming perfectly elastic collisions according to the hard sphere model.

A suite of particle-laden channel flow cases, described in Table 1, are used in this work to assess the role of mass loading, which is defined as the ratio of particle mass to fluid mass: $\phi = nm_p/\rho$, where n is the particle number density. Each case is described by its total mass loading ϕ_0, but ϕ varies in time and space for each flow. The Stokes number is approximately the same across the different cases, and its value was chosen to ensure a strong degree of preferential concentration.

The fluid and particle properties are based on the experiments described in Esmaily *et al.* (2020), with a channel geometry instead of a duct. The fluid is air, with $\rho = 1.2$ kg/m^3 and $\mu = 1.87 \times 10^{-5}$ Pa-s. The particles are monodisperse spheres with diameter $D_p = 11.5$ μm. The total mass loading ϕ_0 is varied by changing the number of particles, using a constant particle density of $\rho_p = 8900$ kg/m^3. Across all simulation cases, the fluid mass flux is held constant. As ϕ_0 is increased, Re_τ decreases slightly and then increases, indicating drag reduction or increase, depending on the amount of particles added. The small change in Re_τ also corresponds to a small change in Stokes number, as indicated in Table 1. The Stokes number used in this work is the friction Stokes number, $St^+ = \tau_p/\tau_{visc}$, which is the ratio of the particle relaxation time scale $\tau_p = \rho_p D_p^2/(18\mu)$ to the viscous time scale associated with the wall shear stress $\tau_{visc} = \delta/\sqrt{\tau_w/\rho}$.

All simulation cases use the same domain and boundary conditions. The channel dimensions are $4\pi\delta \times 2\delta \times (4/3)\pi\delta$ (where $\delta = 2$cm), with periodic boundary conditions in x and z, and smooth, no-slip walls in y. A grid resolution of $[N_x, N_y, N_z] = [280, 140, 140]$ was used to resolve the fluid turbulence at reasonable computational cost. The computational grid is stretched in the wall-normal direction and is uniform in homogeneous directions. For the single-phase baseline case, we use 23 grid points below $y^+ = 10$, where y^+ is the wall-normal coordinate normalized by the viscous length scale. The centerline grid resolution is $[\Delta x^+, \Delta y^+, \Delta z^+] = [10.5, 9.1, 7.0]$.

For the statistics reported in the following sections, all simulation cases were run until a steady state was reached. Then, simulations were continued for a minimum of five flow-through times. Eulerian fluid statistics were obtained by averaging continuously throughout this period, as well as over homogeneous directions, and Lagrangian statistics were computed from ten snapshots evenly distributed during the averaging time.

3. Particle tessellation and differential analysis of the particle velocity

3.1. *Voronoi and Delaunay tessellation*

A Delaunay tessellation of the particle positions defines a graph. The dual graph then defines a cell C_p for each point particle, which has the property that all points inside are closer to the particle than to the other particles. For computing the 3D tessellation (Aurenhammer 1991), we apply the Quickhull algorithm (Barber *et al.* 1996) to the particle positions at two consecutive time instants. This is very similar to the Voronoi tessellation, with the exception that instead of using the circumcenter of the Delaunay cell, which is done for Voronoi, we use the center of gravity to define the vertices of the cell. Oujia *et al.* (2022b) showed that this further improves the stability of the numerical method when computing divergence and curl.

3.2. *Definition of divergence and curl*

To compute the divergence of the particle velocity $\mathcal{D}(\boldsymbol{v}_p)$, following the lines of Oujia *et al.* (2020, 2022b), we first compute the local number density averaged over a cell C_p, which is the inverse of the cell volume. Particles satisfy the conservation equation of the number density n: $D_t n = -n\nabla\cdot\boldsymbol{v}_p$, where $D_t = \partial_t + \boldsymbol{v}\cdot\nabla$ is the Lagrangian derivative. Considering two subsequent time instants t^k and $t^{k+1} = t^k + \Delta t$ of the Delaunay tessellation with time step Δt, we can determine the volume change. Thus we obtain the divergence as

$$\mathcal{D}(\boldsymbol{v}_p) = -\frac{1}{n} D_t n \approx \frac{1}{2\Delta t}\left(\frac{1}{V_p^{k+1}} + \frac{1}{V_p^k}\right)(V_p^{k+1} - V_p^k), \tag{3.1}$$

where V_p^k is the tessellation cell volume at t^k.

Similarly, the curl of the particle velocity can be defined by computing the circulation of the velocity field of particles over a cell C_p. This can also be expressed as the divergence of the velocity, which has been projected onto the orthogonal plane of the direction of the curl through the origin and rotated in a direction $\pi/2$ with respect to the direction of the curl. Defining $\boldsymbol{v}_x^\perp = A_x\boldsymbol{v}$, $\boldsymbol{v}_y^\perp = A_y\boldsymbol{v}$ and $\boldsymbol{v}_z^\perp = A_z\boldsymbol{v}$, where A_x, A_y and A_z are rotation matrices around the different axes, the curl of the particle velocity $\mathcal{C}(\boldsymbol{v}_p)$ is obtained by

$$\mathcal{C}(\boldsymbol{v}_p) = \begin{pmatrix} \mathcal{D}\left(-\boldsymbol{v}_{p,x}^\perp\right) \\ \mathcal{D}\left(-\boldsymbol{v}_{p,y}^\perp\right) \\ \mathcal{D}\left(-\boldsymbol{v}_{p,z}^\perp\right) \end{pmatrix}. \tag{3.2}$$

For more details and a thorough validation in the case of one-way coupled particle-laden isotropic turbulence, we refer to Oujia *et al.* (2020, 2022b). When computing statistics of curl, the mean shear and symmetry in the wall-normal direction must be accounted for. The z-component of curl, $\mathcal{C}_z$, is dominated by mean shear ($d\overline{u}/dy$), which changes sign at $y = \delta$. For this reason, in the statistics that follow, $\mathcal{C}_z$ is used in the bottom half of the channel, and its negative is used in the top half.

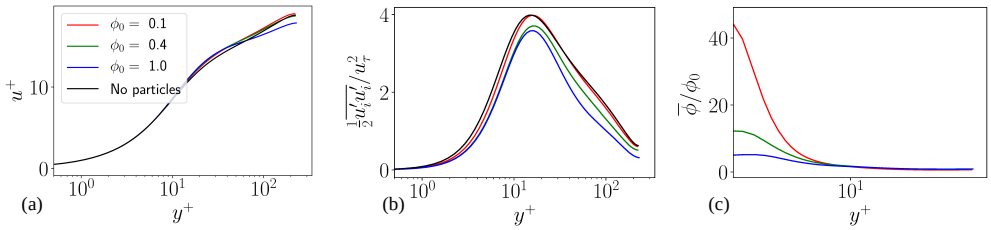

FIGURE 1. (a) Mean streamwise fluid velocity, u^+, as a function of wall-normal distance, y^+, for various mass loadings, as well as without particles. (b) Fluid phase turbulent kinetic energy. (c) Local mean mass loading. The legend in panel (a) applies to all subfigures.

4. Results

In four-way coupled turbulent channel flow, particles alter the fluid velocity, both in the mean and fluctuations. In addition, particles tend to accumulate near the channel walls due to turbophoresis (Reeks 1983; Marchioli & Soldati 2002). Figure 1 shows the degree of these changes depending on the mass loading. The mass loading decreases the velocity gradient in the log layer, with greater effect at larger mass loading. In terms of turbulence, the presence of particles generally attenuates fluid-phase turbulent kinetic energy (TKE), as shown in Figure 1(b), with greater attenuation as ϕ_0 is increased. Because of two-way coupling, the particle phase velocity fluctuations (not shown here) are similarly attenuated. Figure 1(c) shows the local mass loading normalized by the total mass loading, which peaks very close to the wall due to the effect of turbophoresis. As mass loading is increased, collisions are more frequent, disrupting the tendency to accumulate near the wall. At lower values of ϕ_0, this results in stronger gradients in mass loading through the viscous sublayer and a greater difference in mass loading from near-wall to centerline.

Next, we examine the effect of mass loading on particle phase Lagrangian statistics. In this section and the following, the channel flow is broken up into three regions based on the wall-normal distance. For this purpose, the viscous sublayer is defined as the region $y^+ = [0, 5]$, the buffer layer is defined as $y^+ = [5, 30]$, and the logarithmic (log) layer is defined as $[y^+ = 50, y/\delta = 1]$. Strictly speaking, this definition includes the wake region as well, but the particle clustering observed in these two regions is very similar.

To gain a qualitative understanding of clustering and particle divergence in the different flow regions and for different mass loadings, Figure 2 shows particle positions colored by divergence in wall-parallel slices. In the viscous sublayer, particles are organized into low-speed streaks, and most particles show zero divergence, meaning they are being transported without clustering. In the regions with nonzero divergence, positive and negative divergence are intermixed, suggesting crossing trajectories and collisions. In the buffer layer, the streaky structures are still visible, but the prevalence of convergence and divergence is greatly increased, and it is concentrated in hairpin-like structures. Finally, in the log layer, the clustering becomes similar to that of moderate Stokes number particles in homogeneous isotropic turbulence (HIT) (Oujia *et al.* 2020). At larger mass loading, there is a greater proportion of zero-divergence particles, particularly in the viscous sublayer and buffer layers. As ϕ_0 is increased, the particles are more densely packed, but the structures remain qualitatively similar. Only $\phi_0 = 0.1, 0.4$ are shown, but the same qualitative trend continues to $\phi_0 = 1$.

To quantify the clustering behavior, Figure 3(a) shows PDFs of modified Voronoi

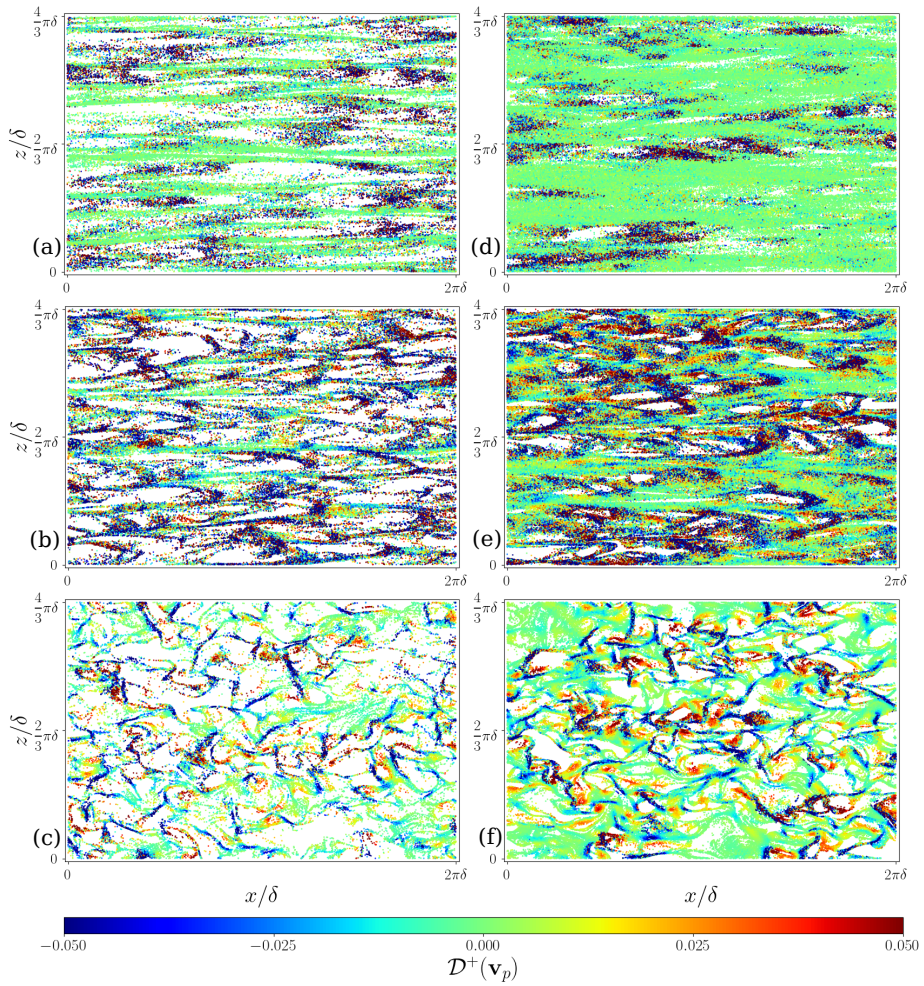

FIGURE 2. Particle positions colored by divergence in wall-parallel slices for (a) viscous sublayer, $\phi_0 = 0.1$; (b) buffer layer, $\phi_0 = 0.1$; (c) log layer, $\phi_0 = 0.1$; (d) viscous sublayer, $\phi_0 = 0.4$; (e) buffer layer, $\phi_0 = 0.4$; and (f) log layer, $\phi_0 = 0.4$. Divergence is normalized by the viscous time scale, and the color bar is truncated to emphasize regions of zero divergence.

volumes for each flow region and mass loadings, normalized by the mean modified Voronoi volume within each layer $\overline{V}_{p,l}$, in order to remove the effect of the wall-normal variation in mass loading. Across the viscous sublayer, buffer, and log layers, there is clear deviation from a random particle distribution with greater probabilities of both clusters and voids (small and large values of $V_{p,l}/\overline{V}_{p,l}$, respectively). The PDFs become noisy at extreme values due to lack of samples. The smallest volumes reported are bound from below by particle collisions. The viscous sublayer distribution is the noisiest at this extreme because of the normalization used. Particles are more densely packed in the viscous sublayer due to turbophoresis, so the average volume in the layer is smaller, shifting the curve to the right relative to other layers.

The distribution of voids is strikingly similar across layers and mass loadings. The viscous sublayer behaves somewhat differently, in that the left side of the PDFs in this

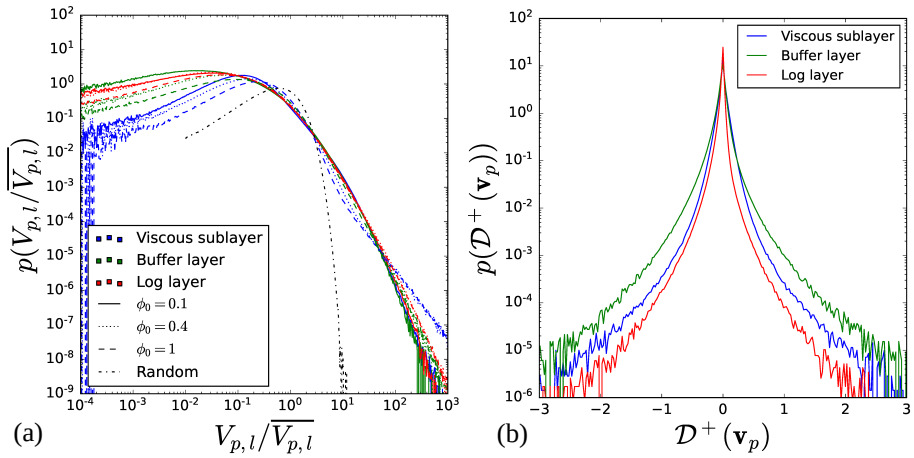

FIGURE 3. (a) PDF of modified Voronoi volume as a function of flow region and mass loading, normalized by the mean modified Voronoi volume within each layer. (b) PDF of particle divergence as a function of flow region for $\phi_0 = 0.1$. The divergence is normalized by the viscous time scale.

ϕ_0	0.1	0.4	1.0
Viscous	6.06×10^{-3}	2.45×10^{-3}	1.79×10^{-3}
Buffer	10.96×10^{-3}	12.12×10^{-3}	9.78×10^{-3}
Log	2.15×10^{-3}	2.54×10^{-3}	2.47×10^{-3}

TABLE 2. Variance of the particle velocity divergence normalized by the viscous time scale for different layers and mass loadings ϕ_0.

zone are closer to a random distribution than are those in other regions. Because particle clusters in the viscous sublayer are dominated by zero-divergence particles in low-speed streaks, we infer that particles in the streaks become nearly randomly distributed due to collisions during their long residence time. This tendency toward random distribution in clusters increases with mass loading, likely due to the increased role of collisions and attenuation of fluid turbulence in the viscous sublayer.

Next, we examine PDFs of particle divergence for $\phi_0 = 0.1$ in Figure 3(b). The variance is largest in the buffer layer, as expected, because the near-wall peak of the fluid turbulent kinetic energy occurs around $y^+ \approx 12$, even with the addition of particles. The buffer layer shows the greatest variance in divergence across all flow cases, as reported in Table 2. In all layers, the divergence distribution exhibits negative skewness, increasing in magnitude away from the wall, indicating a greater likelihood of intense convergence than intense divergence. Additionally, the heavy tails of the PDFs indicate a high prevalence of extreme events, which is expected for inertial particles. At the tails, the PDFs become noisy due to the low frequency of extreme events, which could be improved by averaging over additional flow snapshots.

To highlight the effect of mass loading in the different flow regions on particle divergence, we show PDFs for each region in Figure 4, normalized by the viscous timescale: $\mathcal{D}^+ = \tau_{visc}\mathcal{D}$. In the buffer and log layers, the heavier tails of the PDFs at larger mass loading are evident. This may be due in part to the larger number of particles as ϕ_0 is increased, which offers more sampling to capture extreme events, as described by Oujia *et*

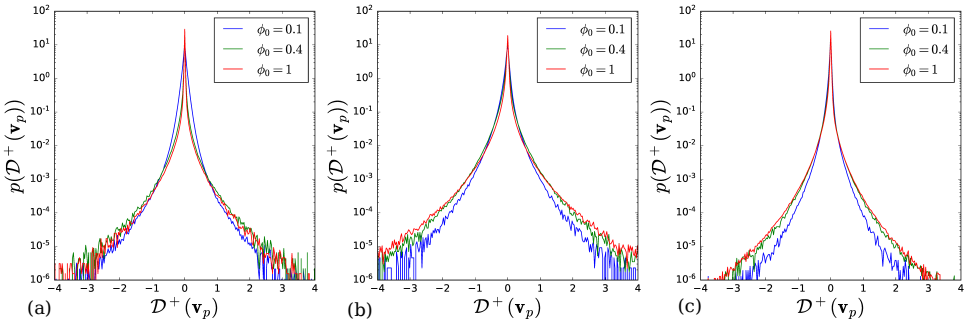

FIGURE 4. PDF of particle divergence, normalized by the viscous time scale, for three different mass loadings in the (a) viscous sublayer, (b) buffer layer, and (c) log layer.

al. (2020). This issue affects the viscous sublayer least, because turbophoresis makes the number density similar there, despite the overall change in mass loading. The variance of the divergence in the viscous sublayer decreases as ϕ_0 increases, which is likely due to the greater fluid turbulent kinetic energy at low mass loading. The greater variance for $\phi_0 = 0.1$ can be seen in Figures 2(a) and 2(d), in which a greater proportion of particles are zero-divergence (green) at the higher mass loading. The changes to particle divergence in the buffer and log layer due to mass loading are less substantial, though there may be a weak maximum in variance at $\phi_0 = 0.4$, as shown in Table 2.

In addition to divergence, the particle velocity curl can be used to characterize the vortical motion of clusters. Figure 5 shows the three components of particle velocity curl across the flow regions. Like the divergence, curl has been normalized by the viscous timescale: $\mathcal{C}^+ = \tau_{visc}\mathcal{C}$. In the viscous and buffer layers, the z-component is clearly asymmetric with a negative mean and nearly symmetric in the log layer. The x and y curl distributions are symmetric across all flow regions. This directional dependence can be explained by the mean shear and homogeneity in x and z. Heavier tails as ϕ_0 is increased are again observed due to increased sampling at larger ϕ_0. The most significant change due to mass loading is observed in the viscous sublayer, where the larger mass loading shows a narrower PDF with strongly decreased likelihood of positive z curl, i.e., locally reversed flow. Narrowing of the distribution is expected based on the tendency of particles to stabilize the near-wall streaks and attenuate velocity fluctuations. Similar to divergence, the particle velocity curl in x and y directions has the greatest variance in the buffer layer, which suggests that stronger particle convergence/divergence is associated with stronger vortical motions.

Another important feature is the anisotropy of the vorticity fluctuations, which can be seen for each flow region in the comparatively narrow PDF of $\mathcal{C}_x$. While a small degree of anisotropy is expected in the log layer for low-Reynolds number channel flow (Andersson *et al.* 2015), the extreme attenuation of C_x relative to the other two components is unique to particle-laden wall turbulence. As ϕ_0 is increased, particle-laden wall turbulence becomes more anisotropic, dominated by streamwise velocity fluctuations (Li *et al.* 2001). Streamwise velocity fluctuations can contribute to vorticity fluctuations in $\mathcal{C}_y$ and $\mathcal{C}_z$ but not $\mathcal{C}_x$, hence the strong attenuation. These effects are present in both fluid and particle vorticity due to the two-way coupling. The fact that the curl is most isotropic in the log layer is also reflected in the particle visualization in Figure 2(c,f), which are qualitatively similar to previous results for HIT (Oujia *et al.* 2020).

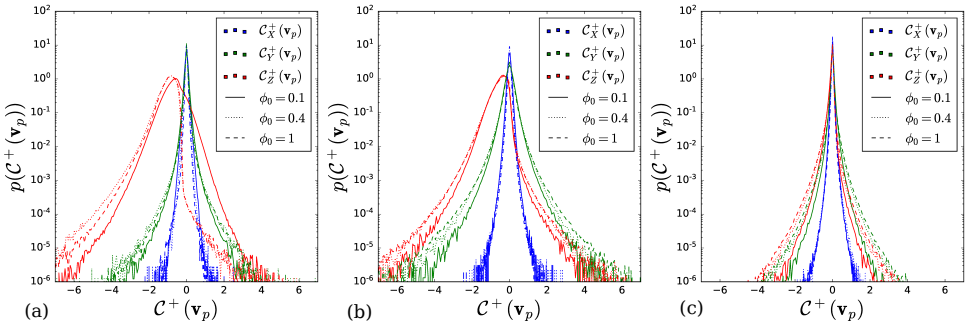

FIGURE 5. PDF of three components of curl, normalized by the viscous time scale, for three different mass loadings in the (a) viscous sublayer, (b) buffer layer, and (c) log layer.

5. Conclusions

In this study, tessellation-based methods for computing particle velocity divergence and curl were applied to four-way coupled channel flow for the first time, and the influence of mass loading and flow region on these quantities was examined in detail. Clustering in the log layer and centerline was found to be qualitatively similar to the previous results for homogeneous isotropic turbulence (HIT) in Oujia *et al.* (2020). Clusters in the viscous sublayer are dominated by low-speed streaks of transported particles which are nearly randomly distributed. Moreover, particle velocity divergence and curl have the greatest variance in the buffer layer, due to the greater strength of turbulent velocity fluctuations there. The influence of mass loading was most strongly observed in the viscous sublayer, where increasing mass loading contributes to reduction in the variance of particle velocity divergence, due to the attenuation in fluid turbulence. Increasing mass loading also narrows the distribution of the spanwise component of curl in the viscous sublayer, which goes along with the stabilization of near-wall streaks as particles are added. It is surprising that a similar attenuation is not observed in the buffer and log layers, although this may be obscured because the number of particles increases with the mass loading, resulting in more sampling of extreme values. The curl of particle velocity was found to be strongly anisotropic in addition to being strongly skewed due to the mean shear. The relative isotropy of the curl in the log layer corresponds with the similarities in clustering between the log layer and HIT.

The focus of the present work has been on differences due to the flow region and mass loading, but in the future, the effect of Stokes number should be considered as well. In addition, wavelet-based statistics can be used to characterize the scale dependence of particle clustering. Finally, the curl and velocity information can be used together to calculate helicity, to characterize swirling particle motions.

Acknowledgments

The authors acknowledge use of computational resources from the Yellowstone cluster awarded by the National Science Foundation to CTR.

REFERENCES

ANDERSSON, H., ZHAO, L. & VARIANO, E. 2015 On the Anisotropic vorticity in turbulent channel flows. *J. Fluids Eng.* **137**, 084503.

Aurenhammer, F. 1991 Voronoi diagramsa survey of a fundamental geometric data structure. *ACM Comput. Surv.* **23**, 345–405.

Barber, C., Dobkin, D. & Huhdanpaa, H. 1996 The quickhull algorithm for convex hulls. *ACM Trans. Math. Softw.* **22**, 469–483.

Basu, P. 2006 Combustion and Gasification in Fluidized Beds, CRC Press.

Esmaily, M. & Horwitz, J. 2018 A correction scheme for two-way coupled point-particle simulations on anisotropic grids. *J. Comput. Phys.* **375**, 960–982.

Esmaily, M., Villafane, L., Banko, A., Iaccarino, G., Eaton, J. & Mani, A. 2020 A benchmark for particle-laden turbulent duct flow: A joint computational and experimental study. *Int. J. Multiph. Flow* **132**, 103410.

Hutter, K. 2005 Geophysical granular and particle-laden flows: review of the field. *Philos. Trans. R. Soc. A* **363**, 1497–1505.

Kulick, J., Fessler, J. & Eaton, J. 1994 Particle response and turbulence modification in fully developed channel flow. *J. Fluid Mech.* **277**, 109–134.

Li, Y., McLaughlin, J., Kontomaris, K. & Portela, L. 2001 Numerical simulation of particle-laden turbulent channel flow. *Phys. Fluids* **13**, 2957–2967.

Marchioli, C. & Soldati, A. 2002 Mechanisms for particle transfer and segregation in a turbulent boundary layer. *J. Fluid Mech.* **468**, 283–315.

Matsuda, K., Onishi, R., Kurose, R. & Komori, S. 2012 Turbulence effect on cloud radiation. *Phys. Rev. Lett.* **108**, 224502.

Monchaux, R., Bourgoin, M. & Cartellier, A. 2010 Preferential concentration of heavy particles: A Voronoi analysis. *Phys. Fluids* **22**, 103304.

Nilsen, C., Andersson, H. & Zhao, L. 2013 A Voronoi analysis of preferential concentration in a vertical channel flow. *Phys. Fluids* **25**, 115108.

Oujia, T., Matsuda, K. & Schneider, K. 2020 Divergence and convergence of inertial particles in high-Reynolds-number turbulence. *J. Fluid Mech.* **905**, A14.

Oujia, T., Matsuda, K. & Schneider, K. 2022a Extreme divergence and rotation values of the inertial particle velocity in high Reynolds number turbulence using Delaunay tessellation. *12th International Symposium on Turbulence and Shear Flow Phenomena (TSFP12), July 2022, Osaka, Japan.*

Oujia, T., Matsuda, K. & Schneider, K. 2022b Computing differential operators of the particle velocity in moving particle clouds using tessellations. *arXiv:2212.03580*, 2022.

Pouransari, H. & Mani, A. 2016 Effects of preferential concentration on heat transfer in particle-based solar receivers. *J. Sol. Energy Eng.* **139**, 021008.

Reeks, M. 1983 The transport of discrete particles in inhomogeneous turbulence. *J. Aerosol Sci.* **14**, 729–739.

Schiller, L. & Naumann, Z. 1935 A drag coefficient correlation. *Zeit. Ver. Deutsch Ing.* **77**, 318–320.

Squires, K. & Eaton, J. 1991 Preferential concentration of particles by turbulence. *Phys. Fluids A* **3**, 1169–1178.